Available online at www.sciencedirect.com

ScienceDirect

Advances in Space Research 61 (2018) 2555–2568

ADVANCES IN SPACE RESEARCH (a COSPAR publication)

www.elsevier.com/locate/asr

Equatorial secondary cosmic ray observatory to study space weather and terrestrial events

Geeta Vichare [a,*], Ankush Bhaskar [a,d], Gauri Datar [a], Anil Raghav [b], K.U. Nair [c], C. Selvaraj [c], M. Ananthi [c], A.K. Sinha [a], M. Paranjape [b], T. Gawade [b], C.P. Anil Kumar [c], C. Panneerselvam [c], S. Sathishkumar [c], S. Gurubaran [a]

[a] *Indian Institute of Geomagnetism, New Panvel, Navi Mumbai 410218, India*
[b] *Department of Physics, University of Mumbai, Santacruz, Mumbai 400098, India*
[c] *Equatorial Geophysical Research Laboratory, Tirunelveli 627011, India*
[d] *Goddard Space Flight Center, NASA, MD 20771, USA*

Received 19 July 2017; received in revised form 26 February 2018; accepted 3 March 2018
Available online 12 March 2018

Abstract

Recently, equatorial secondary cosmic ray observatory has been established at Equatorial Geophysical Research Laboratory (EGRL), Tirunelveli, (Geographic Coordinates: 8.71°N, 77.76°E), to study secondary cosmic rays (SCR) produced due to the interaction of primary cosmic rays with the Earth's atmosphere. EGRL is a regional center of Indian Institute of Geomagnetism (IIG), located near the equator in the Southern part of India. Two NaI(Tl) scintillation detectors are installed inside the temperature controlled environment. One detector is cylindrical in shape of size 7.62 cm × 7.62 cm and another one is rectangular cuboid of 10.16 cm × 10.16 cm × 40.64 cm size. Besides NaI(Tl) detectors, various other research facilities such as the Geomagnetic observatory, Medium Frequency Radar System, Digital Ionosonde, All-sky airglow imager, Atmospheric electricity laboratory to measure the near-Earth atmospheric electric fields are also available at EGRL. With the accessibility of multi- instrument facilities, the objective is set to understand the relationship between SCR and various atmospheric and ionospheric processes, during space weather and terrestrial events.

For gamma-ray spectroscopy, it is important to test the performance of the NaI(Tl) scintillation detectors and to calibrate the gamma-ray spectrum in terms of energy. The present article describes the details of the experimental setup installed near the equator to study cosmic rays, along with the performance testing and calibration of the detectors under various conditions. A systematic shift in the gain is observed with varying temperature of the detector system. It is found that the detector's response to the variations in the temperature is not just linear or non-linear type, but it depends on the history of the variation, indicating temperature hysteresis effects on NaI detector and PMT system. This signifies the importance of isothermal environment while studying SCR flux using NaI(Tl) detectors, especially for the experiments conducted during daytime such as solar eclipses etc.

Keywords: NaI(Tl) scintillation detector; Performance of NaI(Tl); Secondary cosmic ray; Gamma-ray spectroscopy

1. Introduction

The Earth is constantly bombarded by broad energy range cosmic rays (CR). These primary cosmic rays are mainly composed of protons and alpha particles (99%), with a small amount of heavier nuclei (∼1%). Primary cosmic rays come from various sources, including the Sun, supernova explosions, and extremely distant sources such as radio galaxies and quasars. Solar cosmic rays have lower energies (up to about 10^{10} eV per particle) than Galactic cosmic rays (GCR) which have roughly 10^{10} to 10^{18} eV energies.

* Corresponding author.
E-mail address: vicharegeeta@gmail.com (G. Vichare).

https://doi.org/10.1016/j.asr.2018.03.006
0273-1177/

Extremely high energetic (10^{18} eV or higher) particles are the rare extragalactic cosmic rays. The GCR is believed to be accelerated in Supernova Remnant (SNR), but very few in a supernova, while the extragalactic CR mostly in Active Galactic Nuclei (AGN) (Patrignani, et al., 2016).

The flux of incoming cosmic rays at the upper atmosphere is dependent on the solar activity, the Earth's magnetic field, and the energy of the cosmic rays. Geomagnetic cut-off rigidities are a quantitative measure of the shielding provided by the Earth's magnetic field (Bhattacharyya and Mitra, 1997). The cut-off rigidity of any geographic location is a function of the zenith and azimuth angles of arrival, the altitude of the detection location, and the geomagnetic conditions at the time of the measurement. The vertical cut-off rigidity on the Earth's surface in the geomagnetic equatorial regions is ~13–18 GV and essentially zero near the geomagnetic poles. Therefore, a cosmic ray detector operating in the Earth's polar-regions would measure the entire cosmic ray spectrum (limited only by atmospheric absorption), whereas a cosmic ray detector operating in the Earth's equatorial regions would measure only those cosmic ray particles above the geomagnetic cut-off rigidity. However, polar region CR flux contains an additional contribution from solar high energy particles, in contrast to the equatorial regions.

When cosmic rays enter the Earth's atmosphere, they lose their energies by multiple interactions with the atmosphere, which produces a cascade of particles (see Fig. 1) - known as secondary cosmic ray (SCR) particles, a so-called air shower (Patrignani, et al., 2016).

There are various detectors used to measure the SCR flux on the surface of the Earth, such as muon detectors, Neutron monitors, Sodium Iodide detectors, cloud chambers, GM counters etc. (Chilingarian et al. 2005; Mishev et al. 2009). Out of these, Thallium activated NaI detector is an inorganic scintillator, which has high efficiency for gamma rays, adequate energy resolution (~7% at 662 keV) and at the same time, it is cost-effective. Therefore it has been widely used for many years in a variety of fields such as medical, energy resource exploration, industry, nuclear security inspection, high energy particle physics, environmental application etc. As the nuclear radiation is hazardous to the human health, NaI(Tl) scintillation detectors are used in background radiation monitoring systems (Mrdja et al., 2015).

The incident gamma ray interacts with NaI(Tl) detector crystal and transfers its full or partial energy via three processes viz. photoelectric effect, Compton scattering, and pair production. This interaction produces a free electron in the crystal with kinetic energy equal to transfer energy (neglecting work function). The free electron excites a number of electrons proportional to its kinetic energy from the valence band to conduction band of the crystal. The de-excitation of conduction bands emits photons known as fluorescence. An attached photomultiplier tube (PMT) converts the light photon to an electron which is further amplified by multiple dynodes. The electrical voltage signal is collected at the anode through a capacitor, which is further processed by a preamplifier. Finally, the Multi-Channel Analyzer (MCA) through Digital Pulse Processing (DPP), measures the energy of each individual gamma that enters the crystal – this process is called gamma-ray spectroscopy.

NaI scintillation detectors are being used to study the variations in the SCRs produced in the Earth's atmosphere during space weather events, celestial events, solar and lunar eclipses etc. Kandemir (2002) showed that NaI(Tl) can be used to detect the decrease in the SCR flux due to the Earth-crossing of Interplanetary Coronal Mass Ejection (ICME). Using this detector, it has been observed that the SCR flux decreases during solar eclipses, and enhances during lunar eclipse (Kandemir et al., 2000; Nayak et al., 2010; Bhaskar et al., 2011; Raghav et al., 2013). Bhaskar et al. (2011) have shown the possibility of a relation between SCR flux and geomagnetic field variation near equator due to Equatorial Electrojet. Raghav et al. (2015) detected the unusual enhancements in gamma ray counts, which they ascribed to ^{41}Ar emission coming from the nearby nuclear plant. The radon enhancements observed in gamma-ray spectrometers are correlated with the Earthquakes and crustal movements nearby geological faults by many researchers (for example Volodichev et al., 1991). Steinitz et al. (2011) discussed possible effects of solar tides on atmospheric radon signals observed using gamma ray detectors. Katase et al. (1982) showed the diurnal variation of gamma ray lines and found that the diurnal variation of the studied lines is a function of rainfall rate in the region. Further, Nayak et al. (2016) studied the variation in the background gamma ray due to the presence of radioactivity in the rain water. Also, the generation and acceleration of SCR due to thunderstorm activity is observed using scintillation detectors (Alexeenko et al. 2002; Chilingarian et al., 2012, 2015). However, the physical mechanism underlying these variations still remains ambiguous (Shah et al., 1985). A brief overview of the past SCR studies mentioned above implies that the stated problems need continuous measurements of SCR flux and more detailed investigations to resolve them.

Therefore, to study the secondary cosmic rays (SCR), we have installed two NaI(Tl) scintillation detectors at Equatorial Geophysical Research Laboratory (EGRL), Tirunelveli. EGRL is a regional center of Indian Institute of Geomagnetism (IIG), and located near the equator. The energy spectrum of SCR particles produced by the interaction of primary cosmic rays with the atmosphere will be studied in detail during space weather and terrestrial events. However, the most important question to be answered first is why there is a need to have equatorial SCR observatory? Why to study SCR specifically near the equatorial station, EGRL, located at Tirunelveli? These questions are addressed in Section 2. For gamma-ray spectroscopy, it is important to test the performance and energy calibration of the detector. This paper gives the complete details of the SCR observatory setup in Section 3. The results obtained from the performance and calibration testing of NaI(Tl) detectors are presented in sections 4 and 5 respectively. The diurnal trend observed in the atmospheric SCR variations is described in Section 6. The paper ends with the summary in Section 7. The scientific findings using SCR along with other complementary measurements will be followed in the near future.

2. Why to have equatorial SCR observatory (ESCRO)?

2.1. Equatorial ionospheric and atmospheric dynamics

The Equatorial Secondary Cosmic Ray Observatory (ESCRO) has been set up near the equator at Tirunelveli (Geographic Coordinates: 8.71°N, 77.76°E). The geomagnetic coordinates of Tirunelveli are 0.28°N, 151.01°E, and hence falls in the close vicinity of both the geomagnetic and geographic equators. The site is located at ~30 m above mean sea level. Due to the dominance of horizontal component of the geomagnetic field over the magnetic equator, stronger vertical cut-off geomagnetic rigidities are experienced near the equator, allowing only those cosmic ray particles having energy greater than ~13–18 GeV to enter into the Earth's equatorial atmosphere. Based on the algorithm presented in Smart and Shea (2001), the calculated cut-off rigidity at the site is 17.43 GV (http://cosmos.hwr.arizona.edu). Thus, there are many lower energy CR particles which can penetrate at other latitudes but not at the equator, and hence there is an inherent limitation of CR related observations in the equatorial region. However, the advantage of the equatorial station is that the CR flux entered into the equatorial region is devoid of the contribution from solar originated high energy particles. Moreover, in the equatorial region, due to special geometry of the geomagnetic field lines, many interesting electrodynamical phenomena take place. Near the geomagnetic equator, large electric currents flow in the east–west direction at ~100 km above the ground, called as equatorial electrojet (EEJ) currents. These currents result due to the combined effect of special geometry of geomagnetic field lines and ionospheric dynamo (Vichare et al. 2012) driven by neutral tidal winds. Neutral winds due to solar thermal tides are generated by the heat absorbed by atmospheric ozone, oxygen and water content (Vichare and Rajaram, 2013). It is also known that CRs can ionize the nitrogen and oxygen molecules in the atmosphere, and lead to a number of chemical reactions, causing depletion of ozone, influencing the formation of aerosols and clouds etc. (Usoskin et al., 2004; Calisto et al., 2011; Velinov et al., 2013). Bhaskar et al. (2017) showed that a small contribution from CRs exists in global mean temperature variations. Thus in principle, CRs can modify the atmospheric composition and to some extent the heat budget of the atmosphere, which eventually can alter the atmospheric tidal activity and ionospheric electrodynamics. Therefore, studying SCR near the equator to explore the role of cosmic rays in modulating the equatorial ionospheric and atmospheric dynamics is an important aspect of the intended study.

During space weather events such as coronal mass ejections (CMEs), co-rotating interacting regions (CIRs), solar energetic particles (SEPs), solar flares etc., the primary CR count entering the Earth's environment gets affected. As a result, the SCR observed on the ground can get altered, e.g. passage of CMEs results in a decrease of GCR count, and hence a decrease in the SCR count followed by a slow recovery is observed, which is termed as Forbush Decrease (FD) (Forbush 1937; Raghav et al., 2014; Bhaskar et al., 2016a,b). Thus, the temporal modulation of SCR flux is observed during transient space weather events, indicating that the extra-terrestrial activity can influence the SCR count observed on the ground. During geomagnetic storms, strong ring currents flow in the equatorial plane. It would be interesting to study whether the magnetic fields associated with these strong currents can affect the SCR count. The effects reflected in SCR associated with geomagnetic storms can be explored through the data collected at ESCRO.

2.2. Lightning discharges

Tirunelveli is located in the southern part of the Indian peninsula and mainly experience North-east monsoon. The details about the geography and climatic conditions of the location are described by Panneerselvam et al. (2007). The thunderstorm activity at Tirunelveli is very high and hence it is an ideal location to study the terrestrial events such as lightning discharges etc. In this context, the complementary observations from atmospheric electric circuit experiment would be of immense importance.

2.3. Availability of multi-instrument facility

In addition to SCR experiment, various other research facilities such as the Magnetic observatory, Medium Frequency Radar System, Digital Ionosonde, All-sky airglow imager, Atmospheric electricity laboratory to measure the near-Earth atmospheric electric fields are available at EGRL. To study the small-scale dynamics of the mesosphere-lower thermosphere (MLT) region, an all-sky airglow imager was installed at EGRL (Narayanan et al., 2009). Important results on mean winds and tidal climatologies obtained from the MF radar operated at Tirunelveli are reported by Gurubaran and Rajaram (1999). The details of the atmospheric electricity experiment and digital ionosonde are described in Panneerselvam et al. (2003), Sripathi et al. (2016) respectively.

With the accessibility of multi-instrument facilities, the objective to understand the relationship between SCR and various atmospheric and ionospheric processes, during space weather and terrestrial events can be accomplished.

3. SCR experimental setup

At Equatorial Geophysical Research Laboratory (EGRL), Tirunelveli, two NaI(Tl) scintillation detectors of different sizes are installed during January 2017. The small detector is cylindrical in shape and of size 7.62 cm × 7.62 cm and hereafter called as 'Detector 0'. The other detector is rectangular cuboid of size 10.16 cm × 10.16 cm × 40.64 cm and it is called as 'Detector 1' hereafter. Each detector is mounted on 14-pin photomultiplier tube (PMT) of Hamamatsu make (R10233) and the whole assembly is completely sealed by steel for protection. Each PMT is attached to the preamplifier. To remove the stray noise, both the detectors are wrapped using thin aluminum foil and grounded. The outputs of both the detectors are processed and recorded in the computer.

3.1. Housing and shielding of detectors

Since the primary goal of the experiment is to measure the gamma rays coming from the atmosphere, the detectors are kept in an open area. A platform of size 4.27 m × 3.66 m is constructed at the height of 1.83 m from the ground. The platform is raised on five pillars- four side pillars and one central pillar. The central pillar is of dimension 0.61 m × 0.61 m, while side pillars are of 0.3 m × 0.3 m size. To minimize the thermal electronic noise due to the ambient temperature variations, an air-tight, temperature controlled cabin of size 3.66 m × 3.66 m × 0.61 m is constructed on the elevated platform (Fig. 2a). The sketch of this structure with dimensions is shown in Fig. 3. The outer box comprises a double walled structure, with an air gap of 11.43 cm. Further, to control the temperature variations, water bottles and thermocol sheets are kept in the area between the outer box and lead box. The top of the structure is covered by a thin sheet of plywood (25 mm) and thermocol, so that incoming gamma rays would not get attenuated considerably. The details of attenuation due to top cover are presented in section 4.4. Also, the stability of the temperature achieved by this structure is presented in section 4.6. To minimize the effects of humidity on the detectors and PMTs, we have kept silica gel inside the cabin. This air-tight environment, along with silica gel ensures almost steady humidity content inside the cabin.

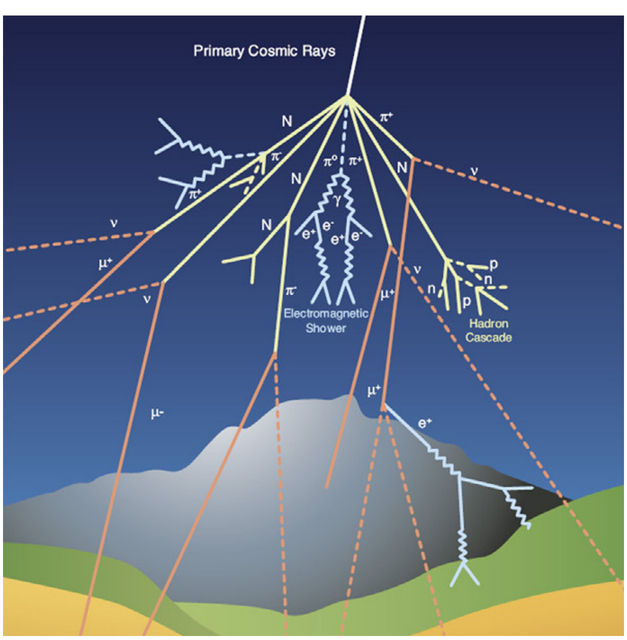

Fig. 1. Air Shower: Interactions of cosmic rays with the Earth's atmospheric particles produce a cascade of secondary cosmic ray particles (SCRs). *Picture produced by Cern.*

Recently, using Monte Carlo simulation model of the atmospheric cascade induced by CRs, Mishev (2016) has estimated the contribution of secondary CR particles to the total radiation at the ground, which is ~10% at sea level. In order to minimize the effects of surrounding radioactivity, mainly of Earth origin, the detectors are surrounded by a thick lead shielding from the bottom and from four sides. For this purpose, we constructed lead shield box of 5 cm thickness, which is open from the top. The dimensions of the lead base are 1.22 m × 1.22 m and four side walls are of height 0.3 m. This ensures that mainly the radiation coming from the top (that is essentially from the atmosphere) will be detected by the detectors. Both the detectors are placed at the center of the lead box (Fig. 2b). The temperature sensor is also placed beside the detectors for recording the temperature in the vicinity of the detectors. The signals from the attached preamplifiers are fed to the MCA kept inside the laboratory about 15 m away from the detectors.

3.2. Multichannel analyzer (MCA) and data acquisition

The multichannel analyzer (MCA) system developed by CAEN, Italy (DT5780 model) is used in the present experiment. It is a compact system that can analyze the signals coming from two detectors independently with 16k channel digital MCA. Also, this system can provide the power to two preamplifiers and high voltage to two PMTs. The digitizer model includes all the blocks from the shaping amplifier to the computer (Fig. 4), and hence provides a very compact digital approach. The parameters used in the MCA are controlled from the computer through a program.

In Multi-Channel Analysis technique, the X-axis of energy histogram can be segmented in "Channels" (or "bins"), each channel representing a pulse height value, in volts (or, if calibrated, the corresponding radiation energy in keV or MeV). The Y-axis values of histogram indicate the number of counts accumulated during the measuring time in the corresponding X-axis channel. The details of the pulse processing can be found at

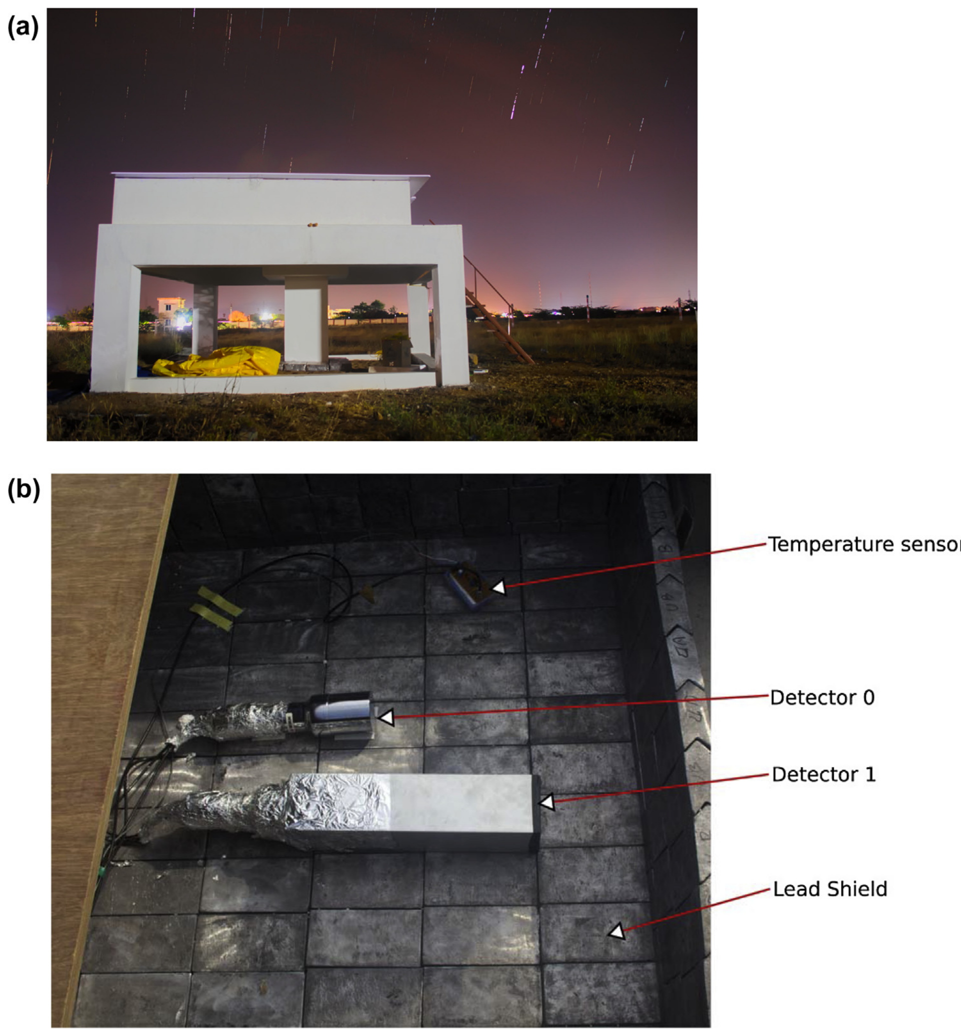

Fig. 2. (a) Air-tight, temperature controlled cabin- site photo. (b) Two detectors along with attached PMTs and preamplifiers are surrounded by lead shield from bottom and four sides, kept inside the temperature controlled cabin. Temperature sensor is also kept to monitor the temperature variations.

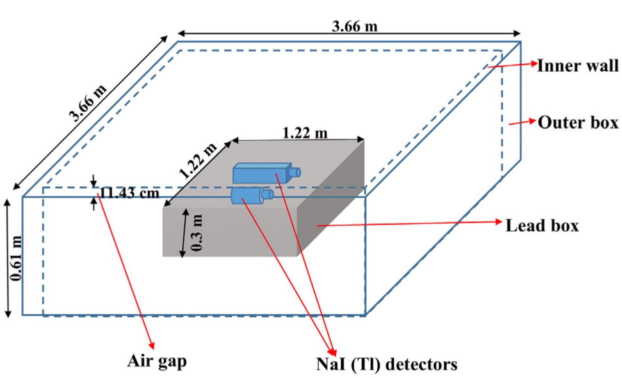

Fig. 3. Sketch of temperature controlled cabin with dimensions.

http://www.caen.it/jsp/Template2/CaenProd.jsp?parent=64&idmod=756. The various parameters are fixed after studying the signal pulse using an oscilloscope (Table 1).

In order to save the energy spectrum automatically after accumulating the spectrum for a desired duration (here one minute), the required modifications are done to the original DPP-PHA (Digital Pulse Processing for Pulse Height Analysis) code provided by CAEN. Thus, the entire set up is made ready to acquire and save the energy spectrum after each minute for both the detectors. The CAEN MCA can be used to carry out coincidence measurements to identify particular nuclear chain reaction happening in the atmosphere. This function will be utilized in future campaign measurements.

4. Performance testing of detectors

The detector performance is characterized by the two most important parameters viz. resolution and efficiency. These characteristics depend on several factors, such as operating high voltage, measured radiation type, intensity, energy etc. To test the performance of NaI(Tl) detectors, we have used ^{137}Cs and ^{60}Co along with the standard gamma-ray lines present in the background radioactivity as sources of gamma radiation (Tables 3 and 4). The intrinsic efficiency, which is the ratio between the flux detected by the detector and the flux emitted by the source is found to be

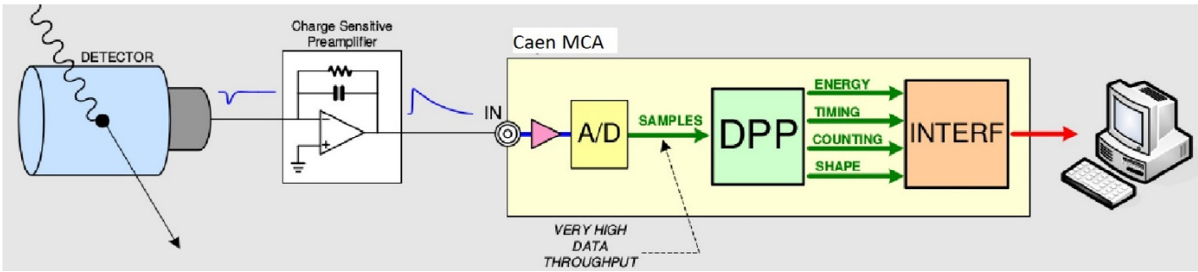

Fig. 4. Block Diagram of a Digitizer-based Spectroscopy System.

Table 1
Parameters set for the experiment.

Parameter	Value
Voltage	700 V
Decay time	50.00 μs
Flat top	1.00 μs
Trapezoid rise time	0.50 μs
Peaking delay	0.50 μs
Input rise time	0.50 μs
Peak hold off	0.60 μs
Trigger hold off	1.30 μs
Energy normalization factor	2.00

Table 2
Percentage reduction in the number of counts under the energy peaks of ^{137}Cs and ^{60}Co due to Plywood.

	Detector 0	Detector 1
^{137}Cs	10.21	10.32
^{60}Co (1.1732 MeV)	10.11	3.33
^{60}Co (1.3325 MeV)	18.98	5.14
Mean %	13.1	6.26

Table 3
Standard sources used in the present study.

Source	γ-Energy (MeV)
137_{Cs}	0.6616
60_{Co}	1.1732, 1.3325

Table 4
Sources identified in the background -spectrum.

Source	γ-Energy (MeV)
Bismuth (^{214}Bi)	1.120, 1.760
Thallium (^{208}Tl)	2.615
Potassium (^{40}K)	1.46

~0.9% for the ^{137}Cs source. The detector testing performed at each stage is elaborated in the following subsections. Firstly, we checked the performance of detectors in terms of efficiency and resolution at different voltages supplied to PMTs, which helps to fix the optimum PMT voltage.

4.1. Voltage dependence of efficiency

In order to get sufficient count rate at the end of the photomultiplier, it is required to apply certain high voltage at each dynode and cathode in PMT. Also, it should be noted that the number of counts does not increase with increasing high voltage, beyond a certain value of high voltage (called as 'Voltage plateau'), achieving maximum efficiency. Therefore, it is important to determine the optimum high voltage to be supplied to the PMT.

For this purpose, we used ^{137}Cs as a gamma ray source, which emits gamma rays of 661 keV energy. We noted the total counts falling under the photo-peak for ^{137}Cs with varying high voltage supplied to PMT. The counts under the photo-peak are calculated using simple integration between the end points of the photo-peak. Fig. 5 shows the total counts under ^{137}Cs photo-peak versus PMT voltage.

The ^{137}Cs photo-peak was not observed at the voltages below 440 V for Detector 0, while it appeared for Detector 1 only after 460 V. But after that, the number of counts increases rapidly with voltage. Beyond threshold voltage of 500 V for Detector 0 and 560 V for Detector 1, the counts remain almost constant at higher voltages. Thus the efficiency of the detector to detect the radiation attains a maximum and remains constant beyond certain voltage. Therefore one can consider 600 V as threshold voltage, beyond which the efficiency of both the detectors remains unchanged.

4.2. Voltage dependence of energy resolution

In radiation spectroscopy, the response of a detector to a mono-energetic source of radiation is very important property and is called as 'energy resolution'. The energy resolution of the detector is limited by uncertainty principle of quantum mechanics and the instrumental profile. The prior one is negligible, but detection mechanism of NaI (Tl) has significant line broadening, which limits the resolution. The energy resolution can be characterized by the full width at half maximum (FWHM), which is defined as the width of the distribution at a level that is just half the maximum ordinate of the peak (Knoll, 1999). This definition assumes that any background or continuum on which the peak may be superimposed is negligible or has been subtracted away. The energy resolution of the detector is conventionally defined as $\% \, Resolution = \frac{FWHM}{Channel\ number\ of\ peak\ centroid,\ H_0} \times 100$.

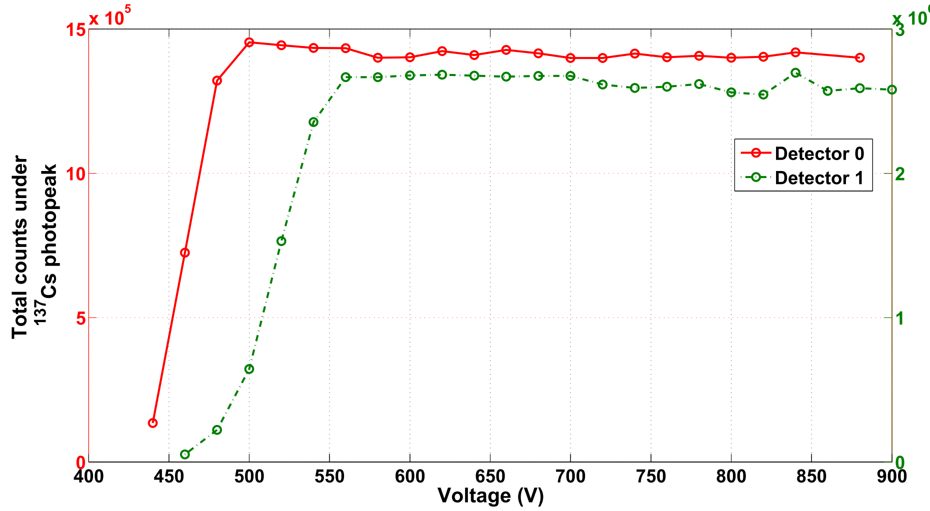

Fig. 5. Total counts under ^{137}Cs photo-peak with varying voltage for both detectors. Scales for Detector 0 (1) are shown on left (right) side.

It can be noted that the smaller value of the energy resolution indicates the better resolving power of the detector, which will enable us to distinguish between two distinct gamma-ray lines whose energies lie close to each other.

We have calculated the energy resolution for both the NaI(Tl) detectors at different PMT voltages (Fig. 6). The energy resolution for Detector 0 is found to be 10.8–8.4%, and that for Detector 1 is 10.8–8.2%. The resolution becomes better for higher voltages. Between ~650–850 V, the energy resolution attains lower values. Considering the results obtained in Figs. 5 and 6, the optimum voltage for both the PMTs is set to 700 V.

4.3. Background spectra and shielding

The radiation detected by the scintillation detector originate from a variety of sources, such as ground radioactivity, man-made concrete buildings, nuclear plants, atmospheric SCRs etc. Since the aim of the proposed experiment is to study the radiation of atmospheric origin, it is required to minimize the contribution from other sources. In order to examine the background radiation at the site of the experiment (Tirunelveli), we studied the background energy spectrum under different conditions, such as:

(i) When the detectors are kept on the ground without shield and without a roof.
(ii) When the detectors are kept on the elevated platform (~2.13 m from ground) inside large double walled box, but without lead shielding and without a roof.
(iii) Same as condition (ii) but with lead shielding applied from all sides except the top.
(iv) Same as condition (iii), but covered with the roof (Plywood of thickness ~2.5 cm).

Fig. 7 displays the background energy spectra, collected for the duration of one hour, under above-mentioned situations. Note that the spectra displayed here are not

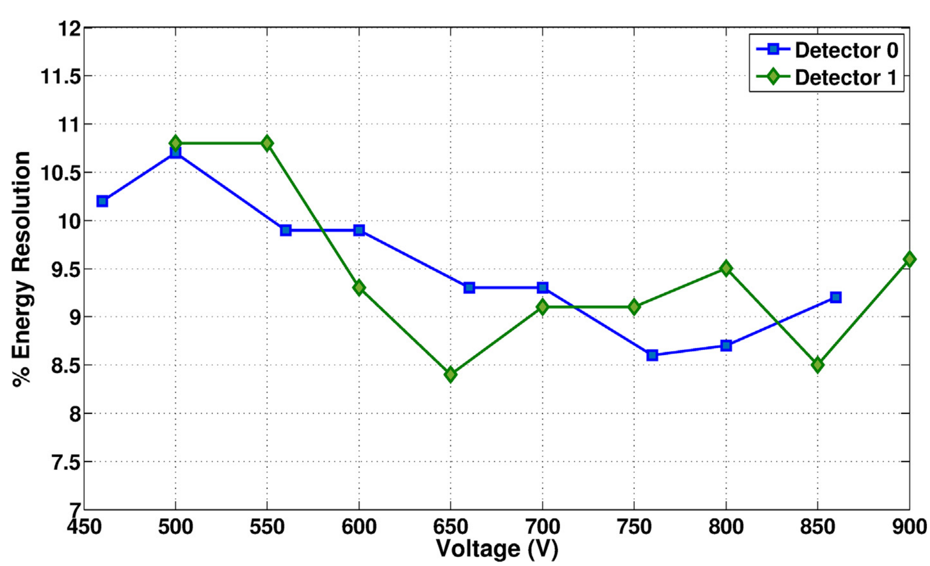

Fig. 6. Energy resolution using ^{137}Cs Source for both the detectors.

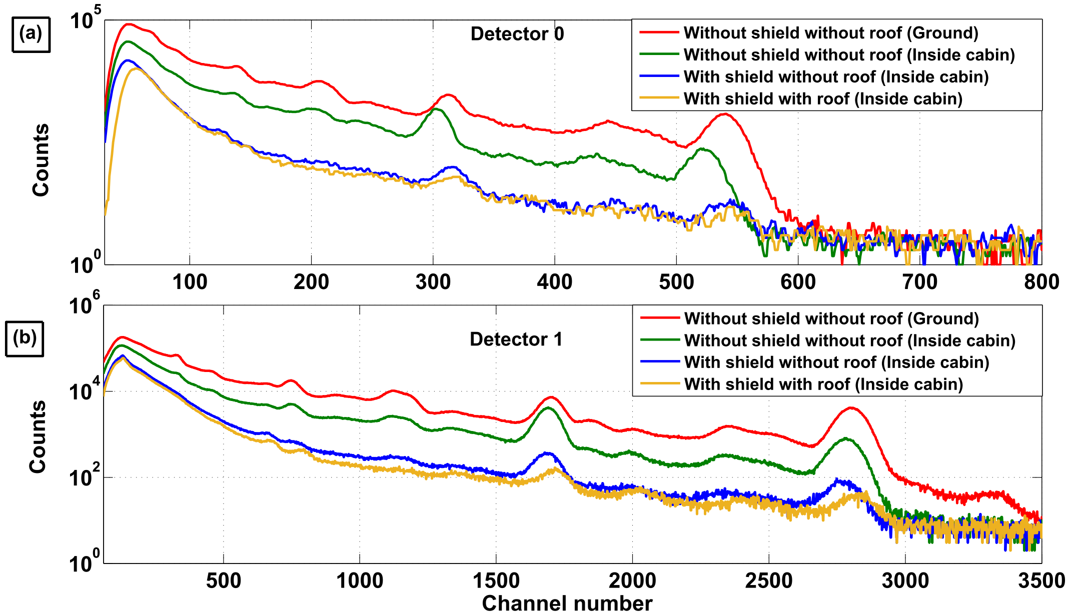

Fig. 7. Background gamma-ray spectra for (a) Detector 0, and (b) Detector 1 at EGRL. Various gamma-ray emission lines are evident in the spectrum as peaks.

calibrated for energies and hence X-axis shows the channel numbers. Nevertheless, two distinct peaks are observed in the background spectra viz. near 300 and 550 channel number for Detector 0, and near 1700 and 2800 channel numbers in Detector 1, which could be attributed to the peaks due to Potassium, ^{40}K (1.46 MeV) and Thallium, ^{208}Tl (2.615 MeV). Also, the energy spectrum at initial channels often shows a sharp rise, which is mainly due to the imposed cut-offs to avoid electronic noise.

It can be clearly noticed that the number of counts decreases from the case (i) to (iv). Interestingly, the count decreases significantly when the detectors are placed on the elevated platform. Now the question arises: whether this decrease in the count is just due to the elevated height from the ground (~2.13 m). Here, one should note that the concrete (RCC) platform of a thickness of 0.3 m, side walls, and central column can also act as shielding from the ground. Therefore, the decrease in the count between case (i) and case (ii) is not merely due to the elevated height.

Further, the count drastically reduces under the influence of lead shielding, by order of two. However, the Potassium and Thallium peaks are still clearly observed, though their intensities have reduced considerably (Note that Y-axis scales are logarithmic). Addition of roof-top has marginally reduced the counts compared to those without the roof condition. The details of the reduction in counts due to plywood roof are discussed in the next section.

4.4. Attenuation due to plywood roof

In order to quantify the percentage of attenuation in the count due to the plywood roof used in the experiment to cover the temperature controlled cabin, we measured the decrease in the number of counts under the photo-peak of ^{137}Cs and two energy peaks of ^{60}Co (see Table 2). For this purpose, we kept the source at a fixed height from the detector, with and without roof conditions. As expected, the number of counts decreases with the presence of overhead plywood roof. The percentage of reduction in the total number of counts is computed with respect to the without roof values. Table 2 shows the percentage of attenuation of the number of counts under ^{137}Cs and ^{60}Co energy peaks for both the detectors. It is evident that the attenuation is very small in case of Detector 1, with ~6% of reduction on an average. The mean value of the reduction is ~13% for Detector 0.

4.5. Gain drift due to temperature variations

NaI(Tl) scintillation detector along with attached PMT and preamplifier are sensitive to the changes in the surrounding temperature, which often results in the shift of the spectrum on the horizontal axis (Reeder and Stromswold, 2004). To study the effect of temperature on the performance of the detector system, we kept both the detectors in the sunlight, so that the temperature of detector/PMT/preamplifier directly varies with atmospheric temperature. The discernible energy peaks associated with Potassium, ^{40}K (1.46 MeV) and Thallium, ^{208}Tl (2.615 MeV) in the background spectrum are identified and the channel numbers corresponding to these energy peaks are noted. Fig. 8 shows the variation of the channel number of ^{40}K and ^{208}Tl peaks as the temperature of both the detectors varies with time (Temperature change by ~18 °C). During this temperature change, the ^{40}K peak drifts by 8 and 20 channel numbers in Detector 0 and 1 respectively. The changes in the channel number of ^{208}Tl peak are 100 and 180 respectively for Detector 0 and 1. Thus we find that the channel number of ^{40}K and ^{208}Tl peaks drift significantly as the temperature of detector system changes. Therefore, it is important to maintain the constant temperature near the detectors, PMTs and preamplifiers. The channel number of an energy peak drifts to lower values with the increase in temperature.

4.6. Temperature stability inside the cabin

As seen in the previous subsection, the gain changes with the temperature of the detector. Therefore, in order to maintain the constant temperature near the detectors, in addition to the double wall structured cabin, materials that are bad conductors of heat are kept between the lead box and the outer cabin. The materials used here are water cans, thermocol and wood sheets, which help to minimize the effect of surrounding temperature change on the detectors placed inside the lead box.

The bottom panel of Fig. 8(b) shows the temperature stability achieved in our experiment. The plots display the temperature recorded by the sensor kept near the detectors inside the cabin and the atmospheric temperature recorded outside by Automatic weather station (AWS). When the outside temperature varies by ~20 °C, the temperature variation inside the cabin is only ~3 °C during the entire course of the day. This implies excellent temperature controlled environment inside the cabin.

Further, we checked the variations in the position of Potassium and Thallium energy-peak locations, when both the detectors are kept inside the cabin. The channel number of each energy peak is noted and plotted against local time (Fig. 8(b)). The plots imply that the curves are almost flat. This suggests that the channel numbers corresponding to each photo-peak do not vary much during the entire day, confirming 'No channel drift'. Thus, the temperature controlled environment assures that there is no gain drift and hence no change in the energy calibration during a day. Also, we perform the calibration procedure every month for 2–3 h on regular basis. For the past 6 months duration, we find almost no variation in the peak channel numbers of the energy sources, indicating that the calibration is stable for the longer time interval as well.

To examine whether the temperature dependence of channel drift is linear or non-linear, we display the scatter plot between the temperature and channel number of energy peak of ^{40}K and ^{208}Tl (Fig. 9). Here the atmospheric temperature recorded by AWS is plotted. The temperature variations of one complete day are considered during the conditions of 'in the sunlight' and 'inside the temperature controlled environment'. The day from the month of March 2017 is shown for the later case, and the experiment in the sunlight was carried out in the month of December 2016. Note that due to cloudy conditions at Tirunelveli in the month of March, the maximum atmospheric temperature was less compared to that during December. The temperature variations have increasing and decreasing trends due to morning rise and afternoon decrease in the temperature. Therefore, we have shown the different phases of the day by different symbols. For the convenience, we have marked pre-sunrise midnight, local sunrise, time of peak temperature, sunset and post-sunset midnight by numbers 1, 2, 3, 4 and 5 respectively. The results 'in the sunlight' condition show very interesting dependence. Instead of just temperature dependence, it shows hysteresis type loops. Both the detectors show nice loops, for the channel shifts of ^{40}K and ^{208}Tl energy peaks. It indicates that the detector's response to the variations in the temperature is not just linear or non-linear type, but it depends on the history of the variation.

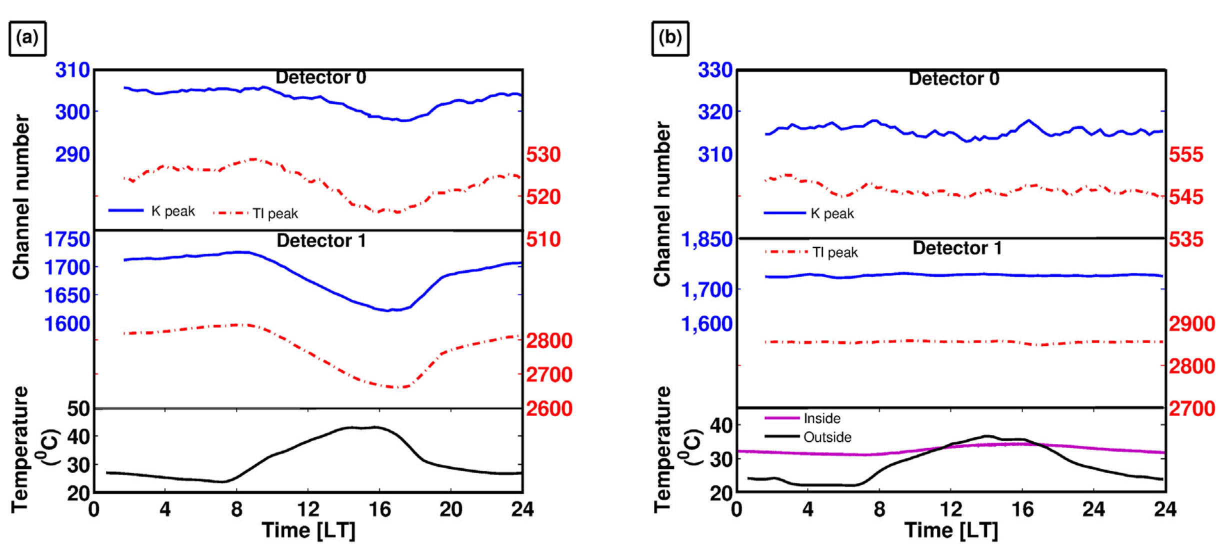

Fig. 8. Gain drift: Variation in the channel number of Potassium and Thallium peaks, when both the detectors are kept (a) in the direct sunlight, (b) inside the temperature controlled environment. The black curve in the bottom panels show the atmospheric temperature from AWS, and pink curve in the right bottom panel shows the temperature variations inside the temperature controlled cabin. (For interpretation of the references to colour in this figure legend, the reader is referred to the web version of this article.)

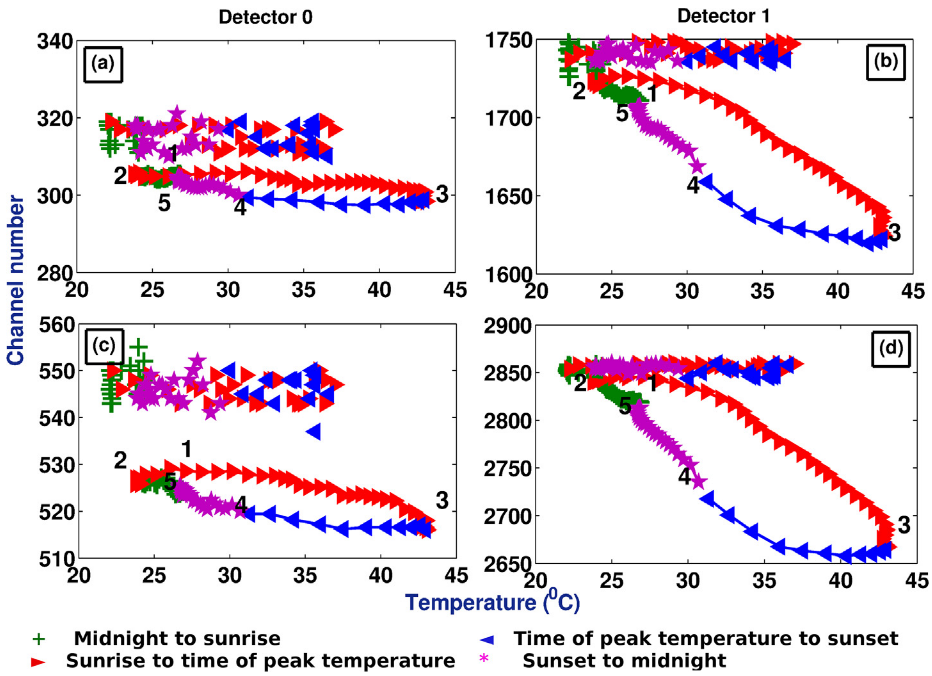

Fig. 9. Scatter plots between Temperature and channel number of energy peak of (a), (b) ^{40}K and (c), (d) ^{208}Tl. Right (left) hand panels for Detector 0 (1). The variations during different phases of day are shown by different symbols. Temperature controlled case is shown by symbols without line, and the case when detectors are kept in the sunlight are shown by symbols connected with lines. Number '1' indicate pre-sunrise midnight, '2' indicate local sunrise, '3' indicates time of peak temperature, '4' indicates local sunset, and '5' indicates post sunset midnight.

It has been observed by the PMT manufacturers that PMTs exhibit a slightly unstable output for several seconds to nearly 1 min after a voltage is applied or light is input, and the output may overshoot or undershoot before reaching a stable level. That means when the incident light or the supplied voltage is changed in a step function, PMT may not produce an output comparable with the same step function, resulting in 'hysteresis' effect (https://www.hamamatsu.com/resources/pdf/etd/PMT_handbook_v3aE-Chapter4.pdf). However, the hysteresis effect reported in the present paper seems to be different than the hysteresis due to unstable output mentioned by the manufacturer. It is challenging to explain the hysteresis effect observed here associated with the temperature changes during entire day and need to be investigated in detail.

The responses under temperature controlled environment are almost flat and do not show hysteresis type variation. This suggests the importance of isothermal environment while conducting experiments with NaI(Tl) detectors during daytime, such as campaigns conducted during solar eclipses.

5. Energy calibration

In gamma-ray spectroscopy, the calibration is necessary in order to interpret the gamma-ray spectrum in terms of energy, rather than channel number. Accurate calibration should involve the use of standard sources with precisely known gamma-ray energies. To account for the non-linearity issues, it is advised to use multiple calibration sources with different gamma lines.

We have used standard gamma-ray sources such as ^{137}Cs and ^{60}Co, which give three energy peaks (Table 3). The background spectra, collected by both the detectors for the duration of one day, show few distinct energy peaks, which are related to Potassium, Thallium and Bismuth (Fig. 10). Therefore, in addition to standard sources of ^{137}Cs and ^{60}Co, we have used a few more energy peaks identified in the background spectrum (Table 4). Note that the energy peaks of ^{40}K (1.46 MeV) and ^{208}Tl (2.615 MeV) appear always very distinctly even in the spectrum of shorter duration. Also, ^{214}Bi (1.76 MeV) is noticeable in the spectra of both the detectors. However, the peak related to ^{214}Bi (1.12 MeV) is not discernible in Detector 0 spectrum, and hence this energy is not used for the calibration of Detector 0. Thus, we have in total seven energy-channel data pairs (3 standard + 4 background) for the calibration of Detector 1 and six data pairs for Detector 0.

Fig. 11 shows the energy against channel number for both the detectors estimated using sources mentioned in Tables 3 and 4. Second-order polynomials are fitted to get the calibration equations mentioned in the plots. The root mean square error (RMSE) values for the calibration curves are 0.0018 and 0.0019 for Detector 0 and Detector 1 respectively, implying the fits are very good.

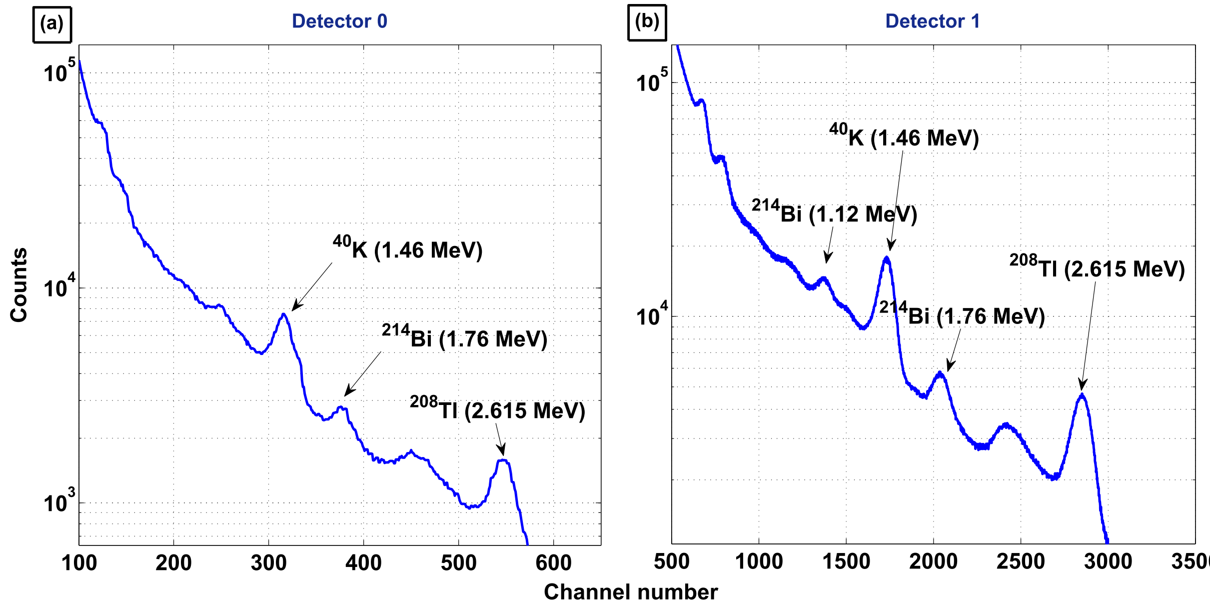

Fig. 10. The energy peaks identified in the background spectrum used for calibration.

6. Diurnal variation of SCR count

It would be interesting to examine whether the energy spectrum obtained after final installation of the detectors inside the temperature controlled cabin have any diurnal variation due to atmospheric parameters such as temperature, humidity, pressure etc. For this purpose, we acquired the total number of counts at each minute. The energy spectrum at lower channels has dominant effects due to scattered gamma radiation from the bottom and surrounding lead shield along with X-rays and electrons.

Therefore, we have considered the number of counts of the channel numbers beyond 100 and 500 for Detector 0 and Detector 1 respectively (Fig. 10). Here as well, for the computation of the total count, we set the lower limit of the channels to 100 and 500 for Detector 0 and Detector 1 respectively, which approximately corresponds to 400 keV energy cut-off. Fig. 12 shows the diurnal patterns obtained using both the detectors. The curves in the top-most panels show the variations on individual days (selected randomly). Note that the diurnal patterns of individual days are vertically shifted for the better visibility. The second panel from the bottom shows the average pattern (blue) with standard deviations (green). The bottom-most panels show the diurnal variations in the atmospheric temperature and humidity. Two vertical black lines indicate sunrise and sunset times, while vertical orange line indicates local noon. Local day time (sunlit hours) are shown by the shaded area.

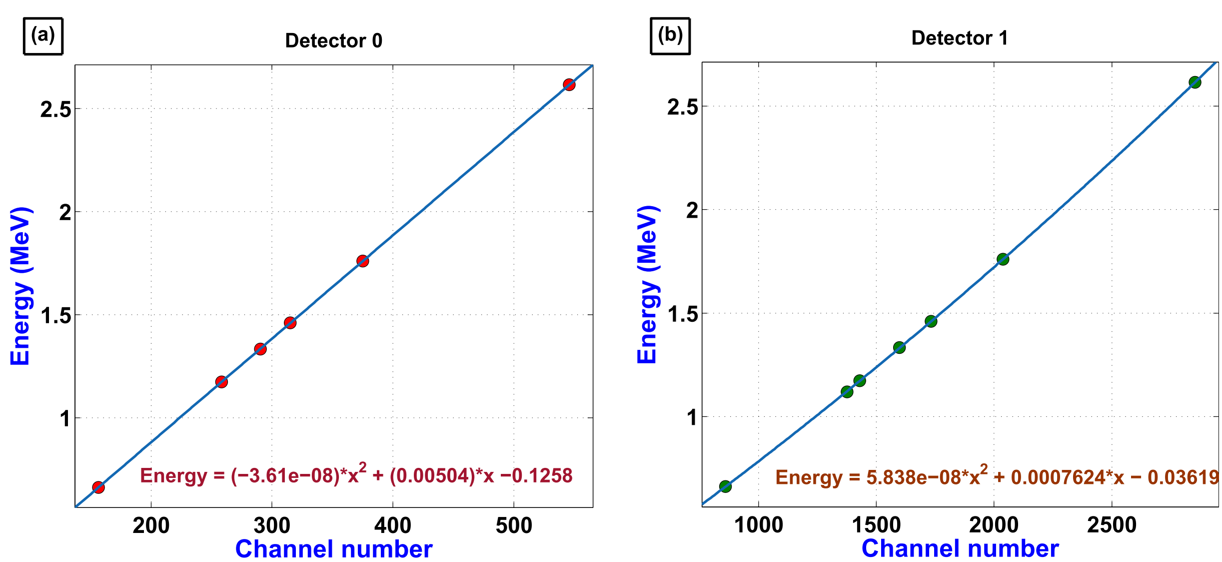

Fig. 11. Energy Calibration for both the NaI (Tl) detectors.

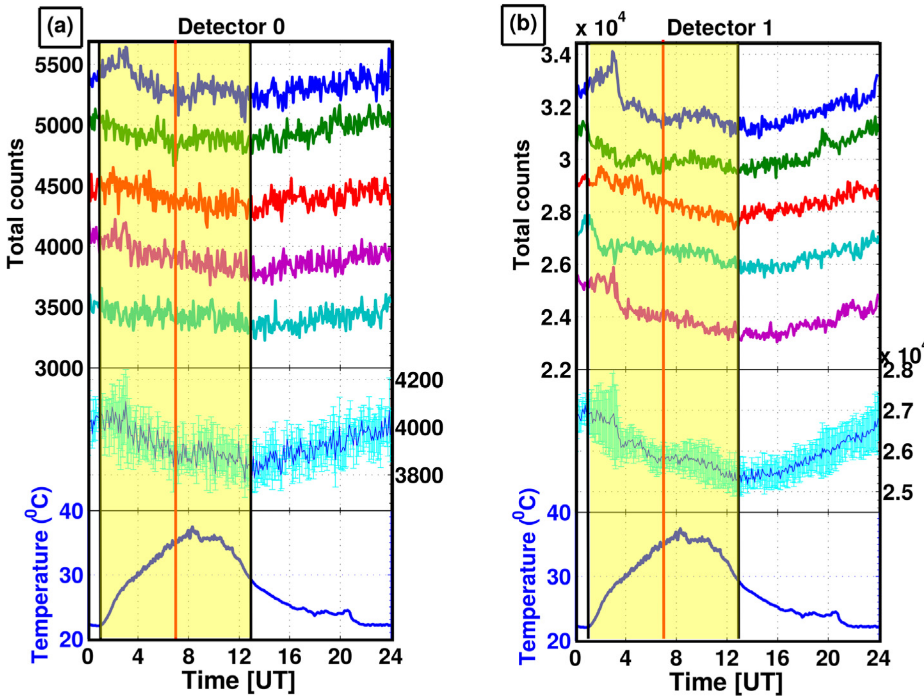

Fig. 12. Diurnal pattern of the total counts of SCR on indivudual days (top panel) and average pattern (middle panel). Temperature (blue) and humidity (pink) variations are displayed in the bottom panel. (a) For Detector 0 and (b) for Detector 1. Two vertical black lines indicate sunrise and sunset times, while vertical orange line indicates local noon. Sunlit hours are shown by shaded area. (For interpretation of the references to colour in this figure legend, the reader is referred to the web version of this article.)

The plots clearly indicate the existence of the diurnal pattern in both the detectors. The total count decreases during the daytime, and starts recovering after the sunset. It seems that the diurnal pattern does not have a direct relationship with the temperature and humidity. However, it can be noted that the SCR measurements presented here are not corrected for the atmospheric pressure, though the detectors are kept in the enclosed environment with constant temperature, volume and pressure. It may be possible that the pattern depicted here is associated with the atmospheric pressure variations (Kubancak, et al., 2014), the details will be reported in the upcoming publication.

7. Summary

To study the secondary cosmic rays near the equator during space weather and terrestrial events, new secondary cosmic ray observatory, housing two NaI(Tl) scintillation detectors, is set up at EGRL, Tirunelveli, located in the Southern part of India. Two Thallium activated NaI detectors of different sizes are kept inside the elevated, temperature controlled cabin. However, in future we plan to use both the detectors of exactly same size, by replacing the smaller size detector. Present paper studies various characteristics of the detectors such as resolution, efficiency, gain drift due to temperature variations, background radiation at the site, shielding of the background radiation, calibration etc. This enables us to finalize various parameters to be set in the experiment. A systematic shift in the gain is observed with varying temperature of the detector and PMT system. It is found that the detector's response to the variations in the temperature depends on the history of the temperature, indicating temperature hysteresis effects. The temperature controlled cabin ensures almost no instrumental drift in the channel due to temperature variations of the detector and PMT. The testing work performed in the present paper demonstrates the importance of isothermal environment while studying SCR flux using NaI(Tl) detectors, especially for the experiments conducted during daytime such as solar eclipses etc. The energy calibration has shown excellent stability till now. The engaged lead shielding reduces the background radiation effectively (order of two). The plywood used for covering the temperature controlled cabin is found to reduce the SCR flux slightly ($< 13\%$). There is a systematic diurnal pattern in the SCR count, which does not seem to be directly related to temperature or humidity. However, the inclusion of the barometric pressure correction may provide a clearer picture of the diurnal pattern. Now, the observatory is functioning in the continuous mode and the science data is ready to be utilized for further research in the field of Space and terrestrial physics. While to understand the spectrum at higher energies, and to separate muon flux contribution and gamma-ray flux contribution in the background spectrum, there is a need to utilize Geant4 simulations (Mishev, 2016). Moreover, we need to understand the overall contribution in gamma-ray flux from all possible sources such as Radon, Thorium etc.

Acknowledgement

Authors are thankful to Dr. D. S. Ramesh, Director, IIG, and Dr. A. Misra, Head, Department of Physics, University of Mumbai, India, for providing required resources and facilities during the installation of the set up.

References

Alexeenko, V.V., Khaerdinov, N.S., Lidvansky, A.S., Petkov, V.B., 2002. Transient variations of secondary cosmic rays due to atmospheric electric field and evidence for pre-lightning particle acceleration. Phys. Lett. A 301 (3–4), 299–306. https://doi.org/10.1016/S0375-9601(02)00981-7.

Bhaskar, Ankush, Purohit, Avadhut, Hemalatha, M., et al., 2011. A study of secondary cosmic ray flux variation during the annular eclipse of 15 January 2010 at Rameswaram, India. Astropart. Phys. 35 (5), 223–229. https://doi.org/10.1016/j.astropartphys.2011.08.003.

Bhaskar, Ankush, Vichare, Geeta, Arunbabu, K.P., Raghav, Anil, 2016a. Role of solar wind speed and interplanetary magnetic field during two-step Forbush decreases caused by Interplanetary Coronal Mass Ejections. Astrophys. Space Sci. 361, 242. https://doi.org/10.1007/s10509-016-2827-8.

Bhaskar, Ankush, Subramanian, Prasad, Vichare, Geeta, 2016b. relative contribution of the magnetic field barrier and solar wind speed in ICME-associated Forbush decreases. Astrophys. J. 828 (2), 104. https://doi.org/10.3847/0004-637X/828/2/104, 8pp.

Bhaskar, Ankush, Ramesh, Durbha Sai, Vichare, Geeta, Triven Koganti, S., Gurubaran, 2017. Quantitative assessment of drivers of recent global temperature variability: an information theoretic approach. Clim. Dyn. 49 (11–12), 3877–3886. https://doi.org/10.1007/s00382-017-3549-5.

Bhattacharyya, A., Mitra, B., 1997. Changes in cosmic ray cut-off rigidities due to secular variations of the geomagnetic field. Ann. Geophys. 15 (6), 734–739. https://doi.org/10.1007/s00585-997-0734-6.

Calisto, M., Usoskin, I., Rozanov, E., Peter, T., 2011. Influence of Galactic Cosmic Rays on atmospheric composition and dynamics. Atmos. Chem. Phys. 11, 4547–4556. https://doi.org/10.5194/acp-11-4547-2011.

Chilingarian, A.K., Arakelyan, K., Avakyan, K., et al., 2005. Correlated measurements of secondary cosmic ray fluxes by the Aragats Space-Environmental Center monitors. Nucl. Instrum. Meth. Phys. Res. A 543, 483–496. https://doi.org/10.1016/j.nima.2004.12.021.

Chilingarian, Ashot, Mailyan, Bagrat, Vanyan, Levon, 2012. Recovering of the energy spectra of electrons and gamma rays coming from the thunderclouds. Atmos. Res. 114–115, 1–16. https://doi.org/10.1016/j.atmosres.2012.05.008.

Chilingarian, A., Chilingaryan, S., Reymers, A., 2015. Atmospheric discharges and particle fluxes. J. Geophys. Res. Space Phys. 120 (7), 5845–5853. https://doi.org/10.1002/2015JA021259.

Forbush, S.E., 1937. On the effect in cosmic-ray intensity observed during the recent magnetic storm. Phys. Rev. 51, 1108–1109.

Gurubaran, S., Rajaram, R., 1999. Long-term variability in the mesospheric tidal winds observed by MF radar over Tirunelveli (8.7°N; 77.8°E). Geophys. Res. Lett. 27, 943–946. https://doi.org/10.1029/1999GL900171.

Kandemir, G., Guclu, M.C., Geckinli, M., et al., 2000. Variation of cosmic ray intensity during the solar eclipse August 11, 1999. Last Total Solar Eclipse of the Millennium. In: Livingston, W., Özgüç, A. (Eds.), ASP Conference Series, vol. 205. ISBN: 1-58381-032-3, p. 202–207.

Kandemir, G., Geckinli, M., Firat, C., et al., 2002. Cosmic ray intensity variation during a CME. Planet. Space Sci. 50 (5), 633–636. https://doi.org/10.1016/S0032-0633(02)00043-0.

Katase, Akira, Narahara, Yoshinori, Ishihara, Yukihiro, et al., 1982. Variation of intensity of environmental gamma-rays measured with Ge (Li) spectrometer. J. Nucl. Sci. Technol. 19 (11), 918–927. https://doi.org/10.1080/18811248.1982.9734237.

Knoll, Glenn F., 1999. Radiation Detection and Measurement, third ed. John Wiley and Sons, Inc., New York.

Kubancak, J., Ambrozova, I., Bütikofer, R., Kudela, et al., 2014. Liulin silicon semiconductor spectrometers as cosmic ray monitors at the high mountain observatories Jungfraujoch and Lomnicky Stit. J. Instrum. 9, P07018. https://doi.org/10.1088/1748-0221/9/07/P07018.

Mishev, A.L., Stamenov, J.N., Angelov, I.I., Ahababian, N.O., Kirov, I. N., Malamova, E.S., 2009. Cosmic ray studies at Moussala – Past, present and future. Adv. Space Res. 44 (10), 1173–1177. https://doi.org/10.1016/j.asr.2008.11.027.

Mishev, A.L., 2016. Contribution of cosmic ray particles to radiation environment at high mountain altitude: comparison of Monte Carlo simulations with experimental data. J. Environ. Radioact. 153, 15–22. https://doi.org/10.1016/j.jenvrad.2015.12.002.

Mrdja, D., Bikit, I., Bikit, K., et al., 2015. Study of radiation dose induced by cosmic-ray origin low-energy gamma rays and electrons near sea level. J. Atmos. Sol. Terr. Phys. 123, 55–62. https://doi.org/10.1016/j.jastp.2014.12.007.

Narayanan, Lakshmi, V., Gurubaran, S., Emperumal, K., 2009. Imaging observations of upper mesospheric nightglow emissions from Tirunelveli (8.7°N). Indian J. Radio Space Phys. 38, 150–158.

Nayak, Pranaba K., Gupta, Sunil K., Jain, Atul, et al., 2010. A study of the γ-ray flux during the total solar eclipse of 1 August 2008 at Novosibirsk, Russia. Astropart. Phys. 32 (6), 286–293. https://doi.org/10.1016/j.astropartphys.2009.09.006.

Nayak, P.K., Gupta, S.K., Jain, A., et al., 2016. Study of terrestrial γ-ray background in presence of variable radioactivity from rain water. Astropart. Phys. 72, 55–60. https://doi.org/10.1016/j.astropartphys.2015.07.002.

Panneerselvam, C., Nair, K.U., Jeeva, K., Selvaraj, C., Gurubaran, S., Rajaram, R., 2003. A comparative study of atmospheric Maxwell current and electric field from a low latitude station, Tirunelveli. Earth Planets Space 55 (BF03352476), 697–703. https://doi.org/10.1186/BF03352476.

Panneerselvam, C., Nair, K.U., Selvaraj, C., Jeeva, K., Anil Kumar, C.P., Gurubaran, S., 2007. Diurnal variation of Maxwell current over the low-latitude continental station, Tirunelveli, India (8.7°N, 77.8°E). Earth Planets Space 59, 429–435. https://doi.org/10.1186/BF03352704.

Patrignani, C., Agashe, K., Aielli, G., et al., 2016. (Particle Data Group), "Cosmic rays". Chin. Phys. C 40, 100001.

Raghav, Anil, Bhaskar, Ankush, Yadav, Virendra, et al., 2013. Confirmation of secondary cosmic ray flux enhancement during the total lunar eclipse of 10 December 2011. J. Geophys. Res. Space Phys. 118 (10), 6426–6433. https://doi.org/10.1002/2013JA019007.

Raghav, Anil, Bhaskar, Ankush, Lotekar, Ajay, Vichare, Geeta, Yadav, Virendra, 2014. Quantitative understanding of Forbush decrease drivers based on shock-only and CME-only models using global signature of February 14, 1978 event. J. Cosmol. Astropart. Phys. 10, 074. https://doi.org/10.1088/1475-7516/2014/10/074, (2014).

Raghav, A., Bhaskar, A., Yadav, V., et al., 2015. Low energy secondary cosmic ray flux (gamma rays) monitoring and its constrains. Astrophys Space Sci 355, 347–352. https://doi.org/10.1007/s10509-014-2172-8.

Reeder, P.L., Stromswold, D.C., 2004. Performance of Large NaI(Tl) Gamma-Ray Detectors Over Temperature −50 °C to +60 °C". Prepared for the U.S. Department of Energy under Contract DE-AC06-76RL01830, Pacific Northwest National Laboratory Richland, Washington 99352, 2004

Shah, G.N., Razdan, H., Bhat, C.L., Ali, Q.M., 1985. Neutron generation in lightning bolts. Nature 313, 773–775. https://doi.org/10.1038/313773a0.

Smart, D.F., Shea, M.A., 2001. A Comparison of the Tsyganenko Model predicted and measured Geomagnetic cutoff latitudes. Adv. Space Res. 28 (12), 1733–1738. https://doi.org/10.1016/S0273-1177(01)00539-7.

Sripathi, S., Singh, R., Banola, S., Sreekumar, S., Emperumal, K., Selvaraj, C., 2016. Characteristics of the equatorial plasma drifts as obtained by using Canadian Doppler ionosonde over southern tip of India. J. Geophys. Res.: Space Physics 121 (8), 8103–8120. https://doi.org/10.1002/2016JA023088.

Steinitz, G., Piatibratova, O., Kotlarsky, P., 2011. Possible effect of solar tides on radon signals. J. Environ. Radioact. 102 (8), 749–765. https://doi.org/10.1016/j.jenvrad.2011.04.002.

Velinov, Peter I.Y., Asenovski, Simeon, Kudela, Karel, Lastovicka, Jan, Mateev, Lachezar, Mishev, Alexander, Tonev, Peter, 2013. Impact of cosmic rays and solar energetic particles on the Earth's ionosphere and atmosphere. J. Space Weather Space Clim. 3, A14 (17pp). http://doi.org/10.1051/swsc/2013036.

Vichare, Geeta, Ridley, A., Yiğit, E., 2012. Quiet-time low latitude ionospheric electrodynamics in the non-hydrostatic Global Ionosphere-Thermosphere Model. J. Atmos. Sol-Ter. Phys. 80, 161–172. https://doi.org/10.1016/j.jastp.2012.01.009.

Vichare, Geeta, Rajaram, R., 2013. Diurnal and semi-diurnal tidal structures due to O_2, O_3 and H_2O heating. J. Earth Syst. Sci. 122 (5), 1207–1217. https://doi.org/10.1007/s12040-013-0353-4.

Volodichev, N.N., Kuzhevskij, B.M., Nechaev, O. Yu., Panasyuk, M.I., Shavrin, P.I., 1991. Strong increase of neutron flux during 22 July, 1990 Eclipse. In: Proc. 22nd ICRC, Dublin, Irelland, 11–23 August 1991, 3, 689–692.

Usoskin, I.G., Gladysheva, O.G., Kovaltsov, G.A., 2004. Cosmic ray-induced ionization in the atmosphere: spatial and temporal changes. J. Atmos. Sol. Terr. Phys. 66 (18), 1791–1796. https://doi.org/10.1016/j.jastp.2004.07.037.